


ARTICLE

# A molecular recognition feature mediates ribosome-induced SRP-receptor assembly during protein targeting

Yu-Hsien Hwang Fu, Sowmya Chandrasekar, Jae Ho Lee, and Shu-ou Shan 

**Molecular recognition features (MoRFs) provide interaction motifs in intrinsically disordered protein regions to mediate diverse cellular functions. Here we report that a MoRF element, located in the disordered linker domain of the mammalian signal recognition particle (SRP) receptor and conserved among eukaryotes, plays an essential role in sensing the ribosome during cotranslational protein targeting to the endoplasmic reticulum. Loss of the MoRF in the SRP receptor (SR) largely abolishes the ability of the ribosome to activate SRP-SR assembly and impairs cotranslational protein targeting. These results demonstrate a novel role for MoRF elements and provide a mechanism for the ribosome-induced activation of the mammalian SRP pathway. Kinetic analyses and comparison with the bacterial SRP further suggest that the SR MoRF functionally replaces the essential GNRA tetraloop in the bacterial SRP RNA, providing an example for the replacement of RNA function by proteins during the evolution of ancient ribonucleoprotein particles.**

## Introduction

Signal recognition particle (SRP) is a universally conserved targeting machine that cotranslationally delivers the majority of membrane and secretory proteins, which compose nearly 30% of the proteome, to the eukaryotic ER or the bacterial plasma membrane (Akopian et al., 2013; Zhang and Shan, 2014). Targeting initiates when SRP recognizes an N-terminal signal sequence or the first transmembrane domain of a nascent polypeptide emerging from the ribosome exit tunnel. The interaction of SRP with the SRP receptor (SR) recruits the ribosome-nascent chain complex (RNC) to the target membrane, where the RNC is unloaded onto the Sec61p (or SecYEG in bacteria) translocation machinery, and the nascent protein is integrated into or translocated across the membrane. The most conserved components of SRP and SR can be found in bacteria, where SRP is composed of a 4.5S RNA tightly bound to the SRP54 protein (named Ffh in bacteria). SRP54 contains a methionine-rich M-domain that binds signal sequences on the nascent polypeptide and a special GTPase domain, termed NG, that dimerizes with a homologous NG-domain in SR (named FtsY in bacteria). The GTP-dependent interaction of SRP with FtsY is extensively regulated by the signal sequence and 4.5S RNA in the bacterial SRP pathway to enable efficient and selective cotranslational protein targeting (Zhang and Shan, 2014; Shan, 2016).

Specifically, RNCs bearing a functional signal sequence pre-organize SRP into a conformation in which the conserved GNRA (N is A, C, G, or U; R is A or G) tetraloop of the 4.5S RNA is positioned to contact a basic surface on the NG-domain of FtsY; this contributes a key interaction that enables the rapid recruitment of FtsY in response to recognition of the correct cargo (Zhang et al., 2008; Shen and Shan, 2010; Shen et al., 2011).

SRP has undergone an extensive expansion in size and complexity during evolution. The eukaryotic SRP contains a larger 7SL RNA on which five additional protein subunits (SRP19, SRP68/72, and SRP9/14) are assembled. Recent work showed that the interaction between mammalian SRP and SR is accelerated ~100-fold by the 80S ribosome and 20-fold by the signal sequence (Bacher et al., 1996; Mandon et al., 2003; Lee et al., 2018). The ribosome-induced stimulation is eukaryote-specific, and its underlying molecular mechanism remains incompletely understood. Single-molecule measurements showed that the ribosome unlocks SRP from an autoinhibited state and allows SRP to sample an active conformation that is conducive to SR binding (Lee et al., 2018). On the other hand, multiple studies have implicated the eukaryotic SR in interaction with and sensing the ribosome (Bacher et al., 1999; Fulga et al., 2001; Legate and Andrews, 2003; Mandon et al., 2003; Jadhav et al., 2015).

---

Division of Chemistry and Chemical Engineering, California Institute of Technology, Pasadena, CA.

Correspondence to Shu-ou Shan: [sshan@caltech.edu](mailto:sshan@caltech.edu).

© 2019 Hwang Fu et al. This article is distributed under the terms of an Attribution–Noncommercial–Share Alike–No Mirror Sites license for the first six months after the publication date (see <http://www.rupress.org/terms/>). After six months it is available under a Creative Commons License (Attribution–Noncommercial–Share Alike 4.0 International license, as described at <https://creativecommons.org/licenses/by-nc-sa/4.0/>).

While bacterial SR is a single protein in which the NG-domain is preceded by two amphiphilic lipid-binding helices, eukaryotic SR is a heterodimer of SR $\alpha$  and SR $\beta$  subunits. SR $\beta$  is a single-pass transmembrane protein anchored at the ER. SR $\alpha$  binds tightly to SR $\beta$  via its N-terminal X-domain, which is connected to the NG-domain through an ~200-residue intrinsically disordered linker. Eukaryotic SR cosediments with empty 80S ribosomes, and the SR linker is important in mediating ribosome binding (Mandon et al., 2003). More recently, Jadhav et al. (2015) examined two charged segments in the SR linker, channel binding region (CBR; residues 129–176) and ribosome binding region (RBR; residues 205–250; Fig. 1 A), and suggested that RBR is responsible for ribosome binding.

The importance of the SR linker reflects the expansion of intrinsically disordered protein regions (IDRs) in the proteome during the evolution from bacteria to higher eukaryotes (Ward et al., 2004; Oldfield et al., 2005). In contrast to the canonical structure–function paradigm, IDRs mediate critical cellular processes without assuming a preformed stable structure (Oldfield and Dunker, 2014; Latysheva et al., 2015; Wright and Dyson, 2015). IDRs are characterized by low sequence complexity, low conservation, and biased amino acid compositions that promote disorder (Oldfield et al., 2005; Oldfield and Dunker, 2014). These features often lead to low-affinity, transient interactions of IDRs with their binding partners, allowing IDRs to mediate dynamic cellular processes such as signaling, complex assembly, or lipid-droplet formation (van der Lee et al., 2014). IDRs often exert their functions via molecular recognition features (MoRFs), which provide interaction sites with binding partners (Mohan et al., 2006; Mészáros et al., 2009; Disfani et al., 2012; Cumberworth et al., 2013; Fang et al., 2013; Fung et al., 2018). MoRFs are short (10–70-residue) segments in IDRs that undergo disorder-to-order transitions upon binding and have been proposed to help recruit interaction partners to an IDR-mediated molecular hub (Oldfield et al., 2008). However, the disordered nature of IDRs presents major challenges to the elucidation of their structure, dynamics, and activity, and more work is needed to understand the mechanistic principle by which MoRFs mediate diverse cellular functions.

In this study, we used the recently reconstituted human SRP and SR to examine the mechanism by which the mammalian SR senses and responds to the 80S ribosome during cotranslational protein targeting. We identified a conserved MoRF element in the disordered SR linker and showed that it is responsible for accelerating SRP–SR assembly in response to the ribosome. The role of this MoRF element phenocopies that of the GNRA tetraloop in the bacterial 4.5S RNA, which accelerates SRP–FtsY assembly in response to the RNC, whereas the corresponding tetraloop in the mammalian 7SL RNA has lost this stimulatory role. We propose that the MoRF element in mammalian SR functionally replaces the electrostatic tether provided by the bacterial 4.5S RNA during SRP–SR interaction. This and other observations suggest that many functions of the bacterial SRP RNA have been replaced by

protein subunits during the evolution of this ancient ribonucleoprotein particle.

## Results

### A MoRF element in the SR linker is important for SR function

The SR linker contains ~200 residues and is intrinsically disordered. Based on charge distribution and evolutionary conservation, a previous work suggested the presence of two functional segments in the SR linker, CBR (residue 129–176) and RBR (residue 205–250), proposed to regulate the Sec61 $\beta$ –Sec62 interaction and to bind the ribosome, respectively (Jadhav et al., 2015). To identify potential interaction motifs, we analyzed the SR linker sequence using multiple MoRF predictors including ANCHOR, MoRFpred, and MFSPSSMPred (Mészáros et al., 2009; Disfani et al., 2012; Fang et al., 2013). The three algorithms are based on very different approaches. ANCHOR uses a scoring function that estimates the likelihood of sequences to undergo folding upon binding of globular partners. MoRFpred uses a machine-learning algorithm to make predictions based on sequence properties including evolutionary conservation, predicted disorder, and selected physicochemical properties of amino acids such as hydrophobicity and charge. MFSPSSMPred uses an algorithm similar to MoRFpred, but the sequences are prefiltered for conservation. All three programs converged on a predicted MoRF at residues 242–261 (Fig. 1 A). Sequence alignments of SR $\alpha$  from diverse species also showed that the MoRF is the most conserved sequence in the SR linker (Figs. 1 B and S1).

To dissect the functions of the various segments in the SR linker, we generated a set of linker deletion mutants, SRdL, SRdC, SRdR, and SRdM, in which the entire linker, CBR, RBR, and MoRF, respectively, are replaced with (GS)<sub>6</sub> (Fig. 1 C). For in vitro assays, we used a functional soluble SR construct, SR $\alpha$  $\beta$  $\Delta$ TM, in which the dispensable N-terminal transmembrane domain of SR $\beta$  is removed (Fig. 1 C; Ogg et al., 1998; Lee et al., 2018). We first tested these mutants in a cotranslational protein targeting assay, which examines the ability of recombinant, purified SRP and SR to mediate the targeting and insertion of a model SRP substrate, preprolactin (pPL), into ER microsomes. The microsomes were trypsinized and salt washed (trypsinized, salt washed rough ER microsome [TKRM]) to deplete endogenous SRP and SR (see Materials and methods). Deletion of the SR linker severely disrupted the targeting and translocation of pPL (Fig. 1, C and D). Unexpectedly, despite having the smallest deletion in the SR linker, SRdM displayed a stronger defect in SRP-dependent pPL targeting than SRdC and SRdR (Fig. 1, C and D), indicating that the MoRF element contains residues essential for SR function.

To further dissect the potential interactions of the MoRF, we mutated conserved residues in this element (R246, W248, L259, and Y261) to alanines (Fig. 1 B). Both mutants SR(RW/AA) and SR(LY/AA) exhibited modest defects in pPL targeting, and the combination of all four point mutations, SR(RWLY/4A), reproduced the targeting defect of SRdM (Fig. 1, B and E). This result

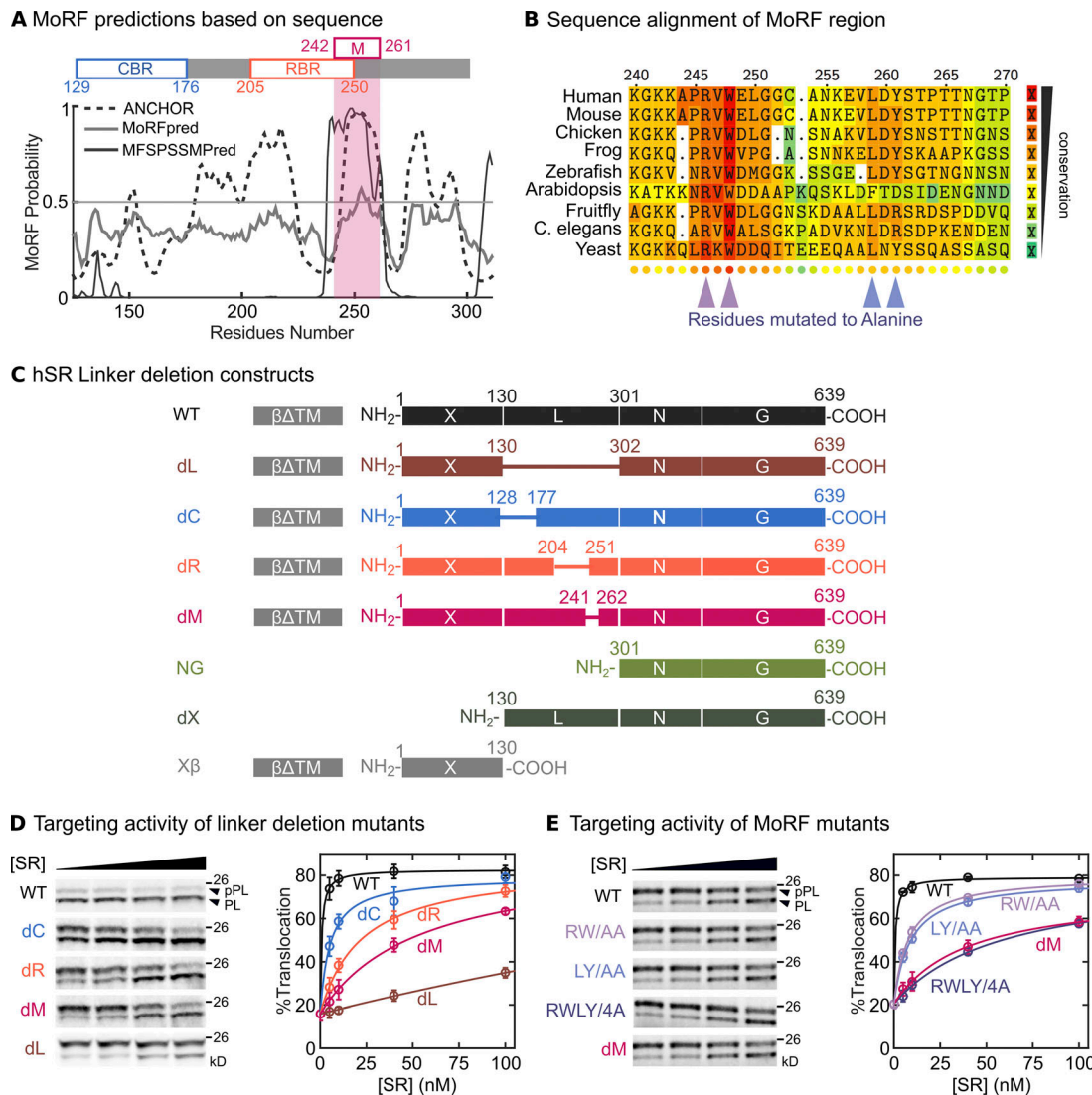


**Figure 1. A conserved MoRF in the SR linker is important for preprotein targeting to ER microsomes. (A)** Probability of MoRF elements in the SR linker generated using the sequence analysis software ANCHOR (dashed line), MoRFPred (gray line), and MFSPSSMPred (black line). A schematic representation of the SR linker is shown above the MoRF probability plot and aligned to the residue index. CBR, RBR, and the predicted MoRF (M) are highlighted. Note that the MoRF partially overlaps with RBR. **(B)** Sequence alignment of the SR MoRF region was generated by T-coffee webserver (Notredame et al., 2000) and plotted using TeXshade package (Beitz, 2000). The arrows indicate the four conserved residues R246, W248, L259, and Y261 in the MoRF. **(C)** Domain structures of WT and mutant SRs used in this study. The transmembrane domain of SRβ was removed to make a soluble SRαβΔTM (Lee et al., 2018), which is denoted as SR for simplicity. In SRdL, SRdC, SRdR, and SRdM, the deleted sequences are replaced by a (GS)<sub>6</sub> linker. **(D and E)** The effects of SR linker deletions (D) and MoRF point mutations (E) on the cotranslational targeting of pPL to TKRM. Representative SDS-PAGE autoradiography images are shown on the left. pPL and PL denote preprolactin and signal sequence-cleaved prolactin, respectively. Translocation efficiencies were calculated from these autoradiographs and their replicates using Eq. 1 in Materials and methods. All values are reported as mean ± SD, with n ≥ 3.

strongly suggests that the conserved aromatic and charged residues in the SR MoRF mediate key molecular interactions during SRP-dependent protein targeting.

**The SR MoRF is important for cotranslational protein targeting in yeast**

To test the role of SR MoRF in vivo, we leveraged the fact that this MoRF element, especially its functionally important RW/LΦ residues identified above, is conserved across eukaryotic organisms including diverse yeast strains (Figs. 1 B and S2 A). Using CRISPR-Cas9-based gene editing, we introduced a (GS)<sub>6</sub>

linker to replace the MoRF sequence (residues 208–230) of genomic *SRP101*, the yeast SR homologue, in *Saccharomyces cerevisiae* strain BY4741 (see Materials and methods). A C-terminal FLAG tag was introduced into both *SRP101* and *srp101<sup>dM</sup>* to facilitate measurement of SR expression levels. To minimize adaptation of yeast cells bearing mutations in components of the SRP pathway (Ogg et al., 1992; Mutka and Walter, 2001; Jiang et al., 2008), the *srp101<sup>dM</sup>* strain was maintained in synthetic minimal medium containing ethanol and glycerol (SEGE). We found that *srp101<sup>dM</sup>* cells exhibited a significant growth defect compared with *SRP101* cells at both 30°C and 37°C (Figs. 2 A and S2 B),

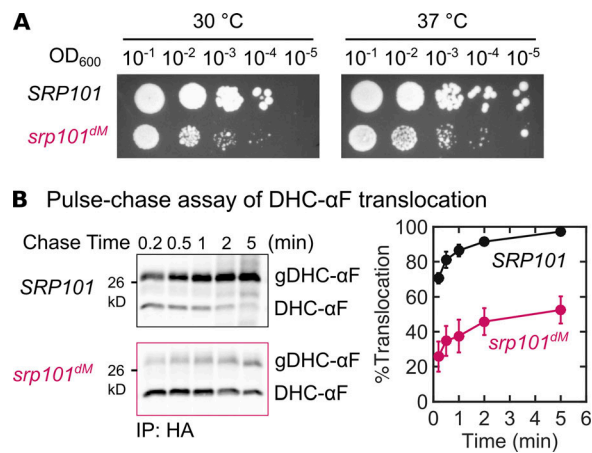


**Figure 2. Mutation of the SR MoRF impairs yeast cell growth and protein translocation into the ER in vivo.** (A) Representative YPD plates showing the growth of *SRP101* and *srp101<sup>ΔM</sup>* cells at 30°C and 37°C. (B) Representative SDS-PAGE autoradiography images (left) and quantification (right) of pulse-chase experiments to measure the targeting and translocation efficiencies of the SRP-dependent model substrate DHC-αF in *SRP101* and *srp101<sup>ΔM</sup>* cells. Successful insertion into the ER results in glycosylation of the substrate (gDHC-αF), which migrates at a higher molecular weight. Translocation efficiencies were calculated from these autoradiographs and their replicates using Eq. 2 in Materials and methods. All values are reported as mean ± SD, with  $n \geq 3$  biological replicates.

indicating that the SR MoRF is important for supporting yeast cell growth.

To test the effect of the SR MoRF deletion on SRP-dependent protein targeting, we measured the in vivo targeting and translocation of a model substrate, DHC-αF, in which the signal sequence of prepro-α-factor is replaced by the hydrophobic core of the dipeptidyl aminopeptidase B signal sequence to convert it into an SRP-dependent substrate protein (Fig. S2 D; Ng et al., 1996; Cho and Shan, 2018). DHC-αF was efficiently glycosylated upon insertion into the ER (Yabal et al., 2003; Wang et al., 2010; Rao et al., 2016), providing a quantitative readout for its targeting and translocation. To measure the targeting kinetics of newly synthesized proteins, we performed pulse-chase assays coupled to immunoprecipitation of HA-tagged substrate proteins (see Materials and methods; Cho and Shan, 2018). The results showed that, while DHC-αF was rapidly and nearly completely translocated in *SRP101* cells, the translocation of DHC-αF was substantially delayed and plateaued at <50% in *srp101<sup>ΔM</sup>* cells (Fig. 2 B). Western blot analysis of yeast ER microsomes showed that the observed targeting defect was not due to a lower level of ER-localized SR in *srp101<sup>ΔM</sup>* compared with *SRP101* cells (Fig. S2 C).

The following observations suggested additional defects in *srp101<sup>ΔM</sup>* cells. In control reactions, we tested the insertion of a posttranslationally targeted model protein substrate, BirA-Bos1, into the ER (Cho and Shan, 2018). BirA-Bos1 is a model tail-anchored membrane protein substrate in which the transmembrane domain of the SNARE protein Bos1 is fused to the C-terminus of BirA (Fig. S2 D). Due to their topology, tail-anchored proteins are targeted after translation via SRP-independent pathways. A significant defect of ER targeting

and insertion was also observed with BirA-Bos1 in *srp101<sup>ΔM</sup>* cells (Fig. S2 E), indicating a general defect in protein insertion into the ER. This is not surprising, as many translocation machineries at the ER are substrates of the SRP pathway; thus, defects of the SRP pathway in *srp101<sup>ΔM</sup>* cells would compromise the biogenesis and function of ER in general. In Western blot analysis, we also found that a fraction of Srp101p<sup>ΔM</sup> was proteolyzed to an ~65-kD fragment (Fig. S2 C). Although partial proteolysis of SRα during ER isolation was well characterized (Meyer and Dobberstein, 1980; Hortsch et al., 1985; Lauffer et al., 1985) and the amount of proteolysis (<50%) was insufficient to account for the observed targeting defect of DHC-αF, the higher proteolytic susceptibility of Srp101p<sup>ΔM</sup> suggests a loss of contacts that protect the SR linker. Together, these results show that the SR MoRF is conserved across eukaryotic organisms, and loss of this element leads to large and promiscuous protein translocation defects of the ER in vivo.

### SR MoRF and the ribosome synergistically stimulate SRP-SR complex formation

To understand the molecular mechanism by which the SR MoRF impacts the targeting reaction, we asked whether the SR MoRF plays a role in SRP-SR complex formation, the first molecular step that the SR participates in during protein targeting. To this end, we first tested the effect of the SR linker mutations on the reciprocally stimulated GTPase reaction between SRP and SR (Fig. 3 A). The GTPase activity of SRP and SR is stimulated 10<sup>2</sup>-10<sup>3</sup>-fold when they form a complex with one another, providing a convenient readout of their interaction (Peluso et al., 2001; Lee et al., 2018). Pre-steady-state fluorescence measurements of the SRP-SR interaction and comparison with the Michaelis-Menten kinetic constants of their stimulated GTPase reaction showed that, at subsaturating SR concentrations, the GTPase rate constant  $k_{cat}/K_m$  is rate-limited by and equal to the rate constant of SRP-SR complex assembly in both the bacterial and mammalian systems (Peluso et al., 2001; Lee et al., 2018). The rate constant at saturating SR concentrations,  $k_{cat}$ , reports on the rate of GTP hydrolysis from a stably formed SRP-SR complex (Fig. 3 A). As the ribosome and signal sequence are required to activate the SRP-SR interaction (Lee et al., 2018), stimulated GTPase reactions between SRP and SR were measured in the presence of saturating 80S ribosome and engineered SRP(4A10L), in which the M-domain of SRP54 is fused to a 4A10L signal sequence. This generates a ribosome- and signal sequence-bound SRP that fully mimics the effect of the RNC in stimulating SRP-SR assembly (Lee et al., 2018).

To decipher the roles of the individual domains of SR in complex assembly, we further tested two SR domain deletion mutants in addition to the linker mutations described above (Fig. 1 C). SRNG contains only the most conserved NG-domain known to mediate dimerization with the homologous NG-domain in SRP54. In SRdX, the X-domain of SRα is deleted, which also abolishes the SRα-SRβ interaction (Fig. 1 C). As reported recently, mutant SRdX is fully functional in mediating rapid recruitment of SR to ribosome and signal sequence-loaded SRP (Lee et al., 2018; Fig. 3 B). In contrast, deletion of the SR linker severely disrupted the SRP-SR

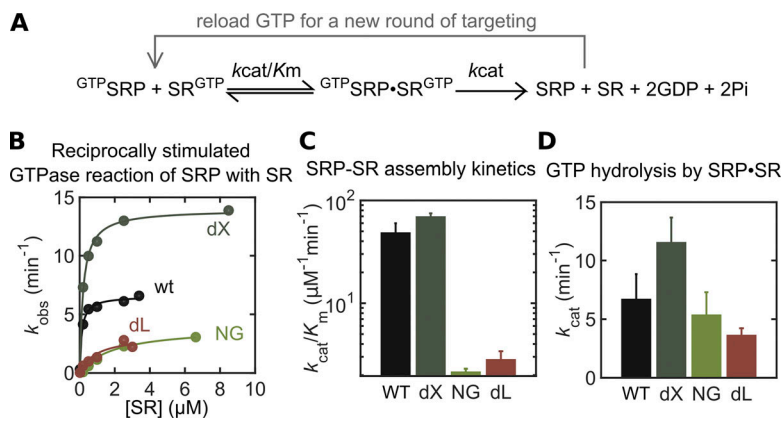


**Figure 3. The SR linker is important for efficient SRP-SR assembly during their reciprocally activated GTPase cycle.** (A) Reaction scheme depicting the GTPase cycle of SRP and SR. SRP and SR are loaded with GTP before their assembly ( $\text{GTPSRP} + \text{SR}^{\text{GTP}}$ ). As GTP hydrolysis ( $k_{\text{cat}}$ ) is much faster than SRP-SR complex dissociation (Peluso et al., 2001; Lee et al., 2018), SRP-SR association is rate limiting for  $k_{\text{cat}}/K_m$  at saturating SR concentrations (Fersht, 1999). The complex dissociates once GTP is hydrolyzed, releasing free SRP and SR to initiate a new round of the GTPase cycle. (B–D) Representative SR concentration dependences of the reciprocally stimulated GTPase reactions between SRP and SR for WT SR and indicated SR mutants (B). The lines are fits of the data to Eq. 3 in Materials and methods, and the obtained  $k_{\text{cat}}/K_m$  and  $k_{\text{cat}}$  values are reported in C and D, respectively. All values are reported as mean  $\pm$  SD, with  $n \geq 2$ .

interaction, reducing the value of  $k_{\text{cat}}/K_m > 20$ -fold (Fig. 3, B and C). The effects of SR linker deletion were similar regardless of whether the SRX $\beta$  domain was present (Fig. 3, cf. SRNG vs. SRdL), indicating that the linker sequence functions independently of the X $\beta$  domain complex (Fig. 3, B and C). In contrast, the value of  $k_{\text{cat}}$  was affected less than twofold by these mutations (Fig. 3, B and D), indicating that the SR linker plays a crucial and specific role in efficient complex formation between SRP and SR but does not substantially affect the GTPase activity of the SRP-SR complex. Importantly, the MoRF deletion led to a similar defect as deletion of RBR or the entire SR linker, reducing the  $k_{\text{cat}}/K_m$  values  $\sim 60$ -fold and the  $k_{\text{cat}}$  value approximately threefold (Fig. 4, A and B, filled circles/bars). In contrast, deletion of CBR led to a modest defect, with an approximately fourfold reduction in  $k_{\text{cat}}/K_m$  and no

effects on  $k_{\text{cat}}$  (Fig. 4, A and B, filled circles/bars). The similar defects of SRdL, SRdR, and SRdM in this assay strongly suggest that the MoRF element is primarily responsible for the role of SR linker in stimulating efficient SRP-SR assembly.

To test whether the SR MoRF is involved in ribosome-induced stimulation of SRP-SR complex assembly, we measured the stimulated GTPase reactions of signal sequence-bound SRP with WT and mutant SRs in the absence of the 80S ribosome (Fig. 4, A and B, open circles/bars). Notably, while the ribosome strongly stimulated complex formation between SRP and WT SR ( $\sim 25$ -fold, Fig. 4 C), as reported (Lee et al., 2018), the stimulatory effect of the ribosome was much smaller, approximately threefold, in reactions with mutants SRdL, SRdR, and SRdM (Fig. 4 C). The loss of ribosome-induced stimulation of SRP-SR assembly is similar between these three mutants, indicating that the MoRF

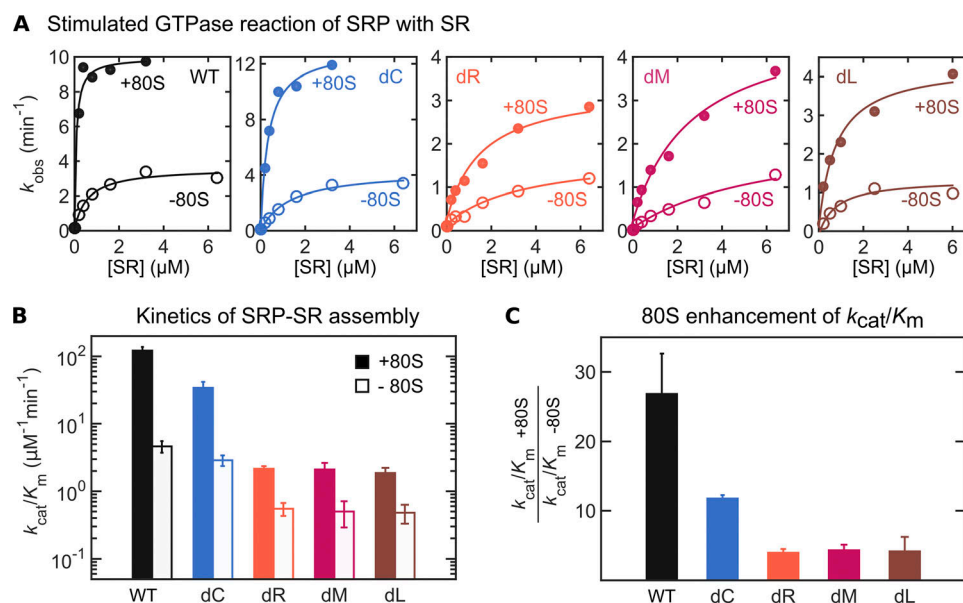
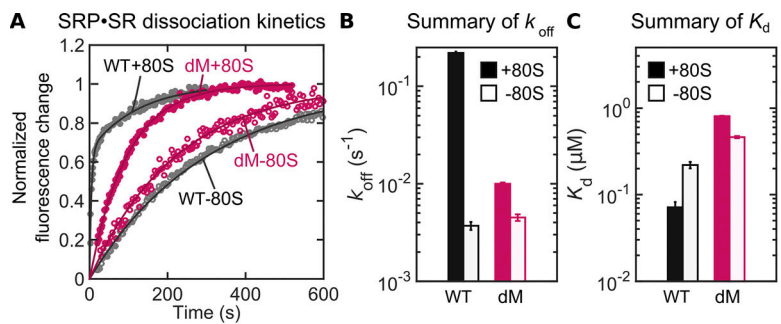


**Figure 4. The SR MoRF is crucial for ribosome-induced activation of SRP-SR assembly.** (A) Representative SR concentration dependences of the reciprocally stimulated GTPase reactions of SRP with WT or mutant SR in the presence (closed circles) and absence (open circles) of ribosome. The lines are fits of the data to Eq. 3 in Materials and methods. (B) Summary of the  $k_{\text{cat}}/K_m$  values from the stimulated GTPase reactions of SRP with WT SR or indicated SR mutants, obtained from the data in A and their replicates. Solid and open bars denote reactions in the presence and absence of the ribosome, respectively. Values are reported as mean  $\pm$  SD, with  $n \geq 2$ . (C) Summary of the stimulatory effects of the ribosome on the  $k_{\text{cat}}/K_m$  values, calculated from the data in B. Values are reported as mean  $\pm$  propagated error, with  $n \geq 2$ .



**D** Summary of the rate and equilibrium constants of the SRP-SR interaction

	+80S		-80S	
	WT	dM	WT	dM
$K_d$ ( $\mu\text{M}$ )	0.071 $\pm$ 0.011	0.809 $\pm$ 0.008	0.220 $\pm$ 0.019	0.463 $\pm$ 0.013
$k_{off}$ ( $\text{s}^{-1}$ )	0.220 $\pm$ 0.0068	0.010 $\pm$ 0.0003	3.7 ( $\pm$ 0.35) $\times 10^{-3}$	4.5 ( $\pm$ 0.35) $\times 10^{-3}$
$k_{on}$ calculated ( $\text{M}^{-1}\text{s}^{-1}$ )	3.09 ( $\pm$ 0.48) $\times 10^6$	1.29 ( $\pm$ 0.04) $\times 10^4$	1.68 ( $\pm$ 0.21) $\times 10^4$	9.72 ( $\pm$ 0.81) $\times 10^3$
$k_{on}$ by $k_{cat}/K_m$ ( $\text{M}^{-1}\text{s}^{-1}$ )	2.0 ( $\pm$ 0.27) $\times 10^6$	3.5 ( $\pm$ 0.89) $\times 10^4$	7.8 ( $\pm$ 1.5) $\times 10^4$	8.4 ( $\pm$ 3.5) $\times 10^3$

element is primarily responsible for communication between the SR linker and the ribosome. In contrast, the ribosome still had a 12-fold stimulatory effect in the reaction with SRdC, only approximately twofold reduced from that of the reaction with WT SR (Fig. 4 C, blue vs. black). These results show that the MoRF in SR linker is a key element that mediates the ribosome-induced activation of SRP-SR complex formation.

**MoRF mediates a transient interaction to stabilize the transition state of SRP-SR assembly**

To test whether the ribosome and MoRF also affect the equilibrium and kinetic stability of the SRP-SR complex, we used an established Förster resonance energy transfer (FRET) assay based on a donor dye (Cy3B) labeled at SRP54(K47C) and an acceptor dye (Atto647N) labeled at the C-terminus of SR. To improve the solubility of labeled SR for fluorescence measurements, we used the SRdX construct in which the SR $\alpha$  X-domain and SR $\beta$  are removed (Fig. S3 A). As previously reported, SRdX displayed SRP-SR assembly, GTPase activation, and preprotein targeting activities comparable to or slightly higher than SR $\alpha\beta\Delta$ TM, and therefore provides a fully functional mimic of SR for studying the initial assembly between SRP and SR (Lee et al., 2018). We also confirmed that the linker deletion mutants (SRdC, SRdR, and SRdM) in the SRdX background had the same effects on the stimulated GTPase reaction as in SR $\alpha\beta\Delta$ TM (Fig. S3 B). This validated the usage of the SRdX constructs to study the role of the MoRF in the fluorescence experiments below.

We first measured the dissociation rate constant ( $k_{off}$ ) of the SRP-SR complex. In the presence of the ribosome, deletion of the MoRF enhanced rather than reduced the kinetic stability of the SRP-SR complex, slowing complex dissociation ~20-fold (Fig. 5, A and B, filled circles/bars). In the absence of the ribosome, however, the MoRF did not significantly affect the kinetic stability of the SRP-SR complex (Fig. 5, A and B, open circles/bars). The effects of the SRdM mutation on SRP-SR complex dissociation rates as well as the synergistic effect of this

**Figure 5. The SR MoRF accelerates both the assembly and disassembly of the SRP-SR complex in the presence of the ribosome.** (A) Representative time courses for dissociation of the SRP-SR complex with WT SR (gray) and mutant SRdM (red) in the presence (+80S, closed circles) and absence (-80S, open circles) of the ribosome. The time courses for WT SR in the presence of the ribosome were fitted to a double exponential equation (Eq. 4 in Materials and methods), and dissociation rate constants of the fast phase were reported. All other time courses were fitted to a single exponential equation (Eq. 5 in Materials and methods). (B) Summary of the dissociation rate constants ( $k_{off}$ ) of the SRP-SR complex formed with WT SR or mutant SRdM in the presence (solid bars) and absence (open bars) of the ribosome. (C) Summary of the equilibrium  $K_d$  of the SRP-SR complex formed with WT SR and mutant SRdM in the presence (solid bars) and absence (open bars) of the ribosome. Values of  $K_d$  were derived from the equilibrium titrations in Fig. S2 C. (D) Summary of the rate and equilibrium constants of the SRP-SR interaction for WT SR and mutant SRdM (dM) in the presence (+80S) and absence (-80S) of the ribosome. All values in B-D are reported as mean  $\pm$  SD, with  $n \geq 3$ .

mutation with the 80S ribosome closely resemble those observed during SRP-SR association (cf. Fig. 5 B vs. Fig. 4 B). Equilibrium titrations using this FRET assay (Fig. S3 C) further revealed that the SRdM mutation modestly weakened the SRP-SR complex, displaying an equilibrium dissociation constant ( $K_d$ ) 10-fold larger than that of WT SR in the presence of the ribosome (Fig. 5, C and D). In the absence of the ribosome, the mutational effect on  $K_d$  is smaller (twofold), reflecting a modest synergy between the MoRF and the ribosome in enhancing the equilibrium stability of the SRP-SR complex (Fig. 5, C and D).

Attempts to measure the SRP-SR association rate constants ( $k_{on}$ ) using the FRET assay were unsuccessful with SRdM, because the mutant SR coaggregated with ribosome at concentrations >1-2  $\mu\text{M}$ . We therefore calculated  $k_{on}$  from the experimentally determined  $k_{off}$  and  $K_d$  values ( $k_{on} = k_{off}/K_d$ ). The calculated  $k_{on}$  values are in reasonable agreement with the values of  $k_{cat}/K_m$  measured from the GTPase reaction and corroborated the conclusions from the enzymatic assay, that is, mutant SRdM slowed SRP-SR association, specifically in the presence of the ribosome, and lost most of the ribosome-mediated activation during this step (Fig. 5 D).

Collectively, these results show that the SR MoRF strongly accelerates complex assembly between SRP and SR (~200-fold), while exerting more modest effects on the kinetic and equilibrium stability of the SRP-SR complex (10–20 fold). Moreover, all the stimulatory effects of the SR MoRF are largely abolished in the absence of the ribosome. Thus, the MoRF element and 80S ribosome act synergistically to stabilize the transition state during SRP-SR complex formation.

**The MoRF does not directly mediate ribosome binding to SR**

The simplest molecular model to explain the synergistic effects of the MoRF and 80S is that MoRF directly recruits the 80S ribosome. To test this model, we examined the effects of SR linker mutations on 80S binding using a cosedimentation assay (Figs. 6

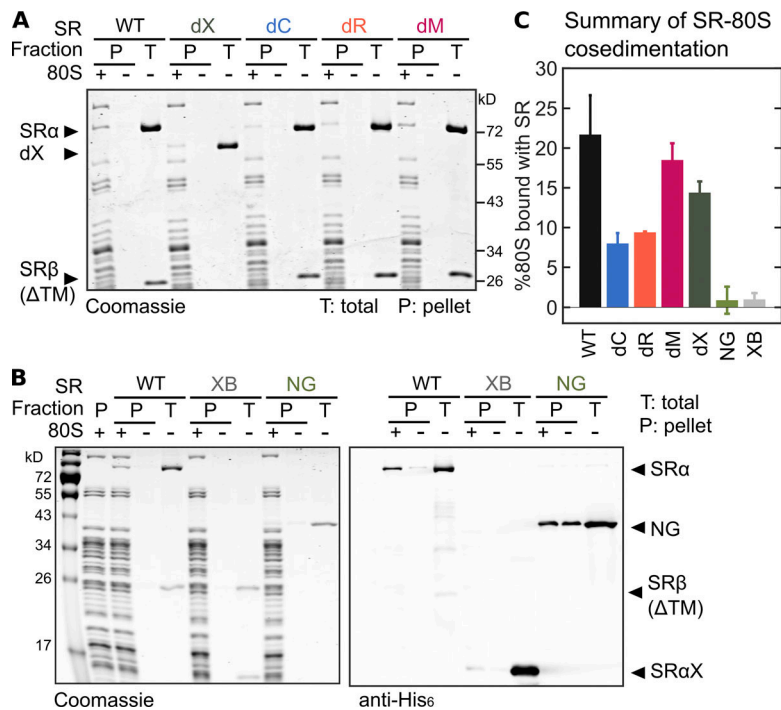


**Figure 6. The SR linker, but not MoRF, mediates the binding of free SR to the ribosome.** (A) A representative Coomassie-stained gel showing the cosedimentation of WT and mutant SRs with the 80S ribosome. P, pellet fraction; T, SR in the total reaction input and used for normalization. (B) Representative Coomassie-stained gel (left) and Western blot analyses (right) showing the cosedimentation of full-length SR and the folded domains in SR with the 80S ribosome. (C) Quantification of the efficiency of SR cosedimentation with the ribosome, based on the fraction of SRα in the pellet fraction relative to the concentration of SRα in the total reaction mix. All values are reported as mean ± SD, with  $n = 2$  for SR-Xβ and SR-NG, and  $n \geq 3$  for all other SR constructs. Replicates of the gel images are shown in Fig. S4.

and S4). Deletion of either the CBR or RBR led to more than twofold reductions in SR-80S binding (Fig. 6, A and C). The folded domains in SR, Xβ, and NG also displayed no detectable 80S binding (Fig. 6, B and C). In contrast, mutant SRdX lacking the Xβ domain complex retained significant ribosome binding. These results suggest that the SR linker is primarily responsible for the interaction of SR with the 80S ribosome, and that both the CBR and RBR in this linker provide important ribosome binding sites. In contrast to the CBR and RBR deletions, deletion of the MoRF led to minimal loss in the 80S binding of SR (Fig. 6, A and C). Thus, the MoRF does not directly recruit the ribosome to SR.

### The electrostatic tethering of SRP RNA to SR is lost in the mammalian SRP pathway

Previous work with the bacterial SRP showed that the conserved GNRA tetraloop of the 4.5S RNA forms an electrostatic interaction with a basic surface on the FtsY NG-domain, providing a transient tether that holds SRP and FtsY together to stabilize the transition state of their assembly (Fig. 7 A, left; Zhang et al., 2008; Shen and Shan, 2010; Shen et al., 2011). The kinetic signatures of the SR MoRF are highly reminiscent of those of the 4.5S RNA tetraloop: both elements accelerate the association and dissociation of the SRP-SR complex, with a much smaller impact on the equilibrium stability of the complex (Shen et al., 2011). Moreover, both the SR MoRF and 4.5S RNA tetraloop specifically exert their stimulatory effects in response to the RNC (Shen et al., 2011). The GNRA tetraloop is conserved in the mammalian 7SL RNA. We therefore asked if the electrostatic tethering interaction between this RNA tetraloop and SR is preserved in the mammalian SRP pathway (Fig. 7 A, right).

To address this question, we assembled SRPs carrying mutations in the GNRA tetraloop and tested their effects on SRP-SR

assembly using the stimulated GTPase assay between SRP and SR. In bacterial SRP, mutation of the RNA tetraloop from GGAA to UUCG reduces the value of  $k_{cat}/K_m \sim 200$ -fold (Zhang et al., 2008). Even modest mutations, such as GUAA and GUCG, led to  $\sim 20$ - and  $\sim 50$ -fold reductions in  $k_{cat}/K_m$ , respectively (Fig. 7 B, *Escherichia coli*). In contrast, the  $k_{cat}/K_m$  value for the reaction of human SRP with SR was minimally affected by any of these tetraloop mutations (Fig. 7 B, mammalian; and Fig. S5 A). Consistent with the results of the GTPase assays, none of the 7SL tetraloop mutations significantly impaired the targeting of pPL to ER microsomes (Fig. S5 B), in contrast to the deleterious effects of the same mutations in the 4.5S RNA (Zhang et al., 2008).

Comparison of the crystal structures of the bacterial and human SRP-SR NG-domain complex further showed that the cluster of basic residues (K399, R402, and K406) on FtsY that comprise the positively charged surface for interaction with the 4.5S RNA tetraloop is reduced to a single K537 in mammalian SR (Fig. S5 C). Moreover, while mutation of K399 in FtsY reduced the rate of SRP-FtsY complex formation  $\sim 100$ -fold (Fig. 7 C, *E. coli*; Shen and Shan, 2010), mutation of the corresponding K537 in mammalian SR had a less than fivefold effect on the rate of SRP-SR assembly (Fig. 7 C, mammalian; and Fig. S5 D). Together, these results show that the mammalian SRP pathway no longer uses the electrostatic tether between the RNA tetraloop and the basic cluster in SR-NG to enable rapid SRP-SR complex formation. Instead, the role of the 4.5S RNA tetraloop is phenocopied by the MoRF element in the SR linker.

### Discussion

In this work, we identified and characterized a highly conserved MoRF element in the disordered linker domain of mammalian SR that specifically accelerates SRP-SR complex assembly in

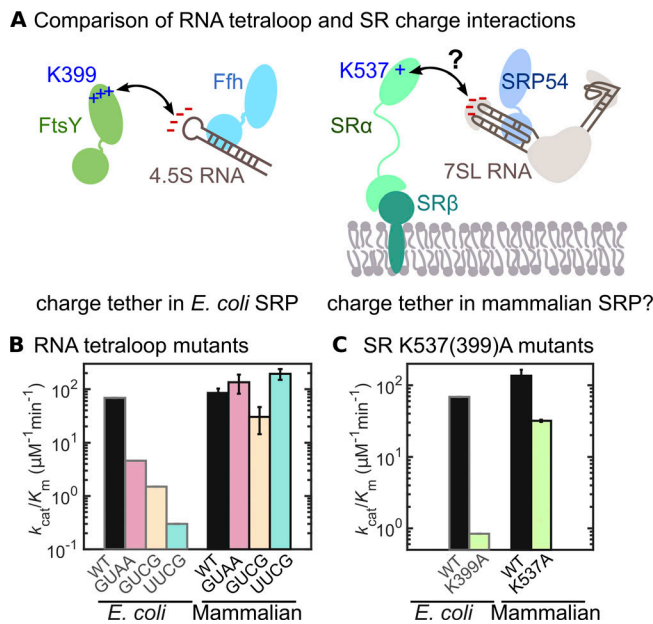


**Figure 7. The RNA tetraloop in mammalian SRP does not play a role in SR recruitment.** (A) Schematics to show the electrostatic tethering interaction between the GGAA tetraloop of bacterial SRP RNA and basic residues on FtsY, and the corresponding residues in the mammalian SRP and SR. The negative charges of the RNA tetraloop are highlighted as red -. The basic surfaces on SR and FtsY are highlighted as blue +. The other subunits in the mammalian SRP are shown in light gray and are not labeled, for simplicity. (B) Summary of the  $k_{cat}/K_m$  values for the stimulated GTPase reactions of mammalian SRP and SR with WT 7SL RNA and the indicated tetraloop mutants. The values are compared with the published  $k_{cat}/K_m$  values for the reactions of *E. coli* SRP and FtsY with WT 4.5S RNA and the same tetraloop mutants (Zhang et al., 2008). (C) Summary of the  $k_{cat}/K_m$  values for the stimulated GTPase reaction of mammalian SRP with WT SR and mutant SR(K537A). The values are compared with the published  $k_{cat}/K_m$  values for the reactions of *E. coli* SRP with WT FtsY and the homologous FtsY(K399A) mutant (Shen et al., 2011). All values in B and C are reported as mean  $\pm$  SD, with  $n \geq 3$ .

response to the ribosome during cotranslational protein targeting. Deletion or mutations of the SR MoRF led to severe defects in protein targeting and translocation to the ER in vitro and in vivo, and resulted in strong growth defects in yeast. Mechanistic dissections showed that the SR MoRF specifically stimulates the recruitment of SR to cargo-loaded SRP, and that its action is synergistic with that of the 80S ribosome. Intriguingly, the roles of the MoRF element in accelerating SRP-SR assembly phenocopy those of the GNRA tetraloop in the bacterial 4.5S RNA, whereas the corresponding RNA tetraloop in the mammalian SRP has lost this essential role.

The kinetic and equilibrium analyses in this work allowed us to construct a free energy diagram that describes the contributions of the ribosome and MoRF to SRP-SR complex formation in a formal model (Fig. 8 A). In the presence of the ribosome, the MoRF specifically stabilizes the transition state of SRP-SR assembly at  $\sim 3.2$  kcal/mol. Both the association and dissociation of the SRP-SR complex are significantly accelerated by the MoRF, whereas the equilibrium of complex formation was affected by only  $\sim 1.4$  kcal/mol (Fig. 8 A, left, comparing black and red lines). The effects of the MoRF are largely lost in

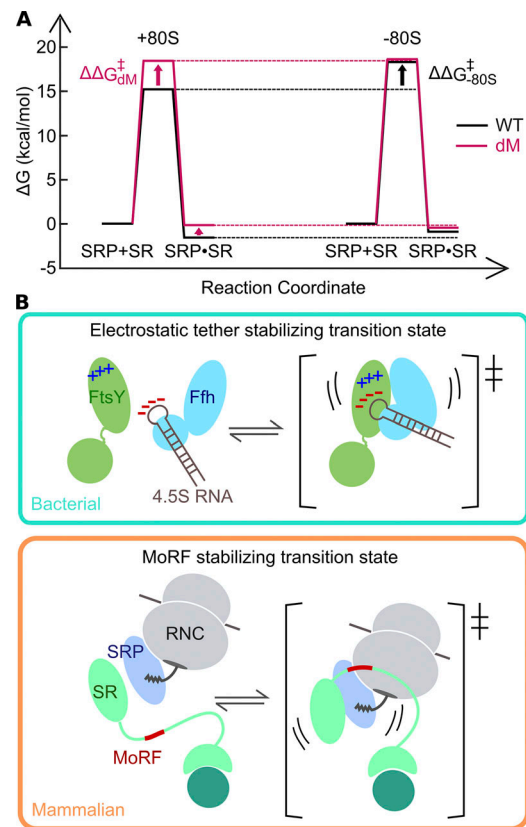


**Figure 8. The SR MoRF stabilizes the transition state of SRP-SR assembly and mimics the role of the bacterial SRP RNA tetraloop.** (A) Free energy profile for SRP-SR complex formation in the presence (left, +80S) and absence (right, -80S) of the ribosome for WT SR (black lines) and mutant SRdM (red lines). Activation energies were calculated from the measured dissociation rate constants ( $k_{off}$ ) and calculated association rate constants ( $k_{on} = k_{off}/K_d$ ) using  $\Delta G^\ddagger = -RT \ln(kh/k_B T)$ , where  $R = 1.986 \text{ cal} \cdot \text{K}^{-1} \cdot \text{mol}^{-1}$ ,  $T = 298 \text{ K}$ ,  $h = 1.58 \times 10^{-37} \text{ kcal} \cdot \text{s}^{-1}$ , and  $k_B = 3.3 \times 10^{-27} \text{ kcal} \cdot \text{K}^{-1}$ , using a standard state of  $1 \mu\text{M}$  SR. (B) Comparison of the role of the 4.5S RNA tetraloop and the SR MoRF in stabilizing the transition state of SRP-SR complex assembly in the bacterial (upper) and mammalian (lower) SRP pathways, respectively. The membrane-embedded region of SR, 7SL RNA, and other SRP subunits are not explicitly depicted for simplicity.

the absence of the ribosome (Fig. 8 A, right, comparing black and red lines). Reciprocally, the ribosome stabilizes the transition state during complex formation with SRP at  $\sim 3.1$  kcal/mol, and has a smaller effect,  $\sim 0.7$  kcal/mol, on the equilibrium of complex formation (WT, black line, comparing +80S and -80S); these stimulatory effects of the ribosome are largely abolished upon deletion of the MoRF (dM, red line, comparing +80S and -80S). Thus, the SR MoRF and the 80S ribosome synergistically activate the assembly between SRP and SR, and they exert their effects specifically during the transition state of complex formation.

Stimulation of SRP-SR complex assembly by the 80S ribosome is a eukaryote-specific phenomenon (Bacher et al., 1996; Mandon et al., 2003; Lee et al., 2018), as is the ability of the eukaryotic SR to directly bind the ribosome (Mandon et al., 2003; Jadhav et al., 2015). Based on the direct interaction of eukaryotic SR with the ribosome, it was proposed that the 80S



ribosome, by contacting both the SRP and SR, could provide a template on which SRP and SR assemble (Mandon et al., 2003; Jadhav et al., 2015). However, the results here indicate that ribosome binding of free SR is largely uncorrelated with the efficiency of SRP-SR complex assembly or cotranslational protein targeting. While SRdC and SRdR showed similarly low affinities for the ribosome, the stimulated GTPase and targeting activities of SRdC are much higher than those of SRdR. On the other hand, deletion of the SR MoRF had minimal impact on SR-ribosome binding but severely disrupted SRP-SR complex assembly and cotranslational protein targeting (cf. Fig. 6 C vs. Figs. 1 D and 4 B). These results ruled out the model that the SR MoRF exerts its stimulatory role by helping to recruit the ribosome. Instead, our results suggest that this element acts at a stage downstream of initial ribosome binding, specifically sensing and transmitting the information from the ribosome to the SRP and SR GTPases to activate their interactions. This could occur by optimizing the positioning of the SR NG-domain with respect to the SRP54-NG near the ribosome exit site to promote their assembly. The enrichment of conserved hydrophobic and aromatic residues in this MoRF also suggests that it participates in key, albeit transient, molecular interactions to exert this positioning effect. The precise interactions mediated by the MoRF remain to be determined.

Intriguingly, mutation of the MoRF in the mammalian SR linker phenocopies the effects of mutations in the 4.5S RNA tetraloop in the bacterial SRP. Both elements (the eukaryotic SR MoRF and the bacterial SRP RNA tetraloop) specifically impact the transition state during SRP-SR assembly, with a much smaller effect on the equilibrium of complex formation (Peluso et al., 2000, 2001; Zhang et al., 2008). The actions of both elements are also strongly synergistic with the cargo (Shen and Shan, 2010; Shen et al., 2011). In bacteria, the RNA tetraloop interacts with the basic surface on the FtsY NG-domain to form a transient electrostatic tether that stabilizes the transition state during complex assembly (Fig. 8 B upper panel; Shen and Shan, 2010; Shen et al., 2011). Mutation of either the charged residues in FtsY or the RNA tetraloop significantly impacts SRP and FtsY interactions (Fig. 7, B and C, *E. coli*; Zhang et al., 2008; Shen and Shan, 2010). In contrast to the bacterial SRP, the assembly of mammalian SRP and SR is not sensitive to either of these mutations (Fig. 7, B and C, mammalian), indicating that the electrostatic tethering via the RNA tetraloop is no longer employed in the mammalian SRP system. Together with the similarities of the effects of SR MoRF and 4.5S RNA tetraloop, we propose that the mammalian SRP uses the SR MoRF in place of the RNA tetraloop to activate rapid SRP-SR assembly in response to cargo binding (Fig. 8 B, lower panel).

In addition to the SRP RNA tetraloop, the functions of multiple other elements in the bacterial SRP RNA are performed by protein subunits in the eukaryotic SRP. For example, the eukaryote-specific SRP9/14 mediates interaction of the Alu-domain at the elongation factor binding site to regulate translation elongation, whereas the Alu-domain of SRP is comprised solely of RNA in Gram-positive bacteria (Halic et al., 2006; Mary et al., 2010; Beckert et al., 2015). Additionally, in a recent structure of a “prehandover” mammalian RNC-SRP-SR ternary

complex, the SRP-SR NG-domain complex moved to the distal site of 7SL RNA after initial assembly and formed a network of interactions with SRP68/72 and the X $\beta$ -domain of SR (Kobayashi et al., 2018). The analogous distal site docking of the NG-domain complex in bacterial SRP is mediated exclusively by interactions with the 4.5S RNA (Ataide et al., 2011). Collectively, these observations support a model in which multiple functions of the SRP RNA in this ancient ribonucleoprotein particle have been replaced by protein subunits during its evolution in higher eukaryotic organisms. MoRF elements in IDRs could play an important role in this process, by virtue of their ability to mediate weak, transient, but specific interactions encoded by their sequence, structural, and dynamic properties.

## Materials and methods

### Vector, protein and RNA preparations

Plasmids for recombinant expression of SRP protein and RNA subunits, SR $\alpha\beta\Delta$ TM, and SRdX have been described (Lee et al., 2018). In brief, hSRP19 and hSRP54-4A10L were expressed in Rossetta pLyS cells using pET15b-h19 and pET23d-h54-4A10L, respectively. hSRP9 and hSRP14 were expressed separately in BL21(DE3)pLysS using pET3b-h9 and pET9a-h14, respectively, and purified as hSRP9/14 complex by combining the clarified lysates. hSRP68 and hSRP72 were coexpressed in BCY123 yeast cells using pRS426-h68/72 vector. pS7CA was used for in vitro transcription of the 7SL SRP RNA. For SR $\alpha\beta\Delta$ TM, SR $\alpha$  and SR $\beta\Delta$ TM were coexpressed in BL21(DE3\*) cells using pET28a-hSR $\alpha$  and pET15b-SR $\beta\Delta$ TM, respectively. SRdX was expressed using pET28a-hSR $\alpha$ (130–639). Plasmids for expression of mutant SRs and mutant 7SL RNAs were constructed using the QuikChange mutagenesis protocol (Stratagene). SRdC, SRdR, SRdM, and SRdL have residues 129–176, 205–250, 242–261, and 131–301, respectively, replaced with (GS)<sub>6</sub>. Recombinant WT and mutant SRs were expressed from *E. coli* and purified as previously described (Lee et al., 2018). Reconstituted SRP and SRP(4A10L) were assembled from individually expressed/purified SRP proteins and in vitro transcribed/gel purified 7SL RNA as described in the previous study (Lee et al., 2018). 80S ribosomes were purified from rabbit reticulocyte lysate as described in Lee et al. (2018). pPL mRNA for in vitro translation-translocation assays were synthesized by in vitro transcription using SP6 polymerase following the Megascript protocol (Ambion). Cyslite SRP54(K47C) was labeled with Cy3B maleimide (Invitrogen) and purified as described (Lee et al., 2018). SRdX and SRdX(R458A) were labeled at the C-terminus with Atto647N (Invitrogen) via sortase-mediated ligation, as described in Lee et al. (2018). SR were centrifuged at 4°C, 100,000 rpm, in a TLA100 rotor (Beckman Coulter) for 30 min to remove aggregates before all biochemical experiments.

### Cotranslational targeting and translocation assay

Assays were performed as described (Lee et al., 2018). Briefly, 8.5  $\mu$ l of in vitro translation reactions of pPL in wheat germ extract (Promega) containing <sup>35</sup>S-methionine were initiated and, within 3 min, added to a mixture of 30 nM SRP; 0, 5, 10, 40, or 100 nM WT or mutant SR; and 0.5 eq/ $\mu$ l of salt-washed,

trypsin-digested microsomal membrane (TKRM) to a total volume of <math><13.5\ \mu\text{l}</math>. Reactions were quenched by addition of 2× SDS-loading buffer and boiling after 40 min and analyzed by SDS-PAGE and autoradiography. The efficiency of translocation was quantified from Eq. 1, in which  $PL$  and  $pPL$  are the integrated intensities for prolactin and preprolactin bands from autoradiography:

$$\% \text{ translocation} = \frac{PL}{PL + \frac{7}{8} \times pPL} \times 100. \quad (1)$$

### Construction of SRP101FLAG and srp101<sup>dM</sup>FLAG strains

Genomic *SRP101* in strain BY4741 was replaced with *SRP101-FLAG* or *srp101<sup>dM</sup>-FLAG* (denoted as *SRP101* and *srp101<sup>dM</sup>* in the text) using CRISPR-Cas9 genome editing (Ryan et al., 2016). First, a DNA fragment containing the *SRP101* ORF and the flanking 5' UTR (524 bp) and 3' UTR (184 bp) was amplified from yeast genomic DNA (BY4741) and cloned into the pUC19 vector. To insert a C-terminal FLAG tag, pCAS-sgRNA<sup>FLAG</sup> plasmid encoding *Streptococcus pyogenes* Cas9 and sgRNA containing a 20-bp reverse guide sequence (5'-TTGTTGAAT AACATTGTCTG-3') that targets the sequence 36 bp downstream of the *SRP101* ORF was cloned. The guide sequence was designed using Benchling CRISPR analysis tool. A flexible linker sequence (GSGAASG) followed by 1×FLAG sequence (DYKDDK) was inserted at the C-terminus of the *SRP101* coding sequence in pUC19, and asynonymous codon substitutions were inserted in the region targeted by the guide sequence using QuikChange Mutagenesis (Stratagene). The resulting plasmid was used to amplify a DNA repair fragment containing the *SRP101-FLAG* coding sequence and ~100 bp of the 3' UTR downstream of the sgRNA<sup>FLAG</sup> site. pCAS-sgRNA<sup>FLAG</sup> plasmid and the linear repair fragment were cotransformed into freshly prepared BY4741 competent cells and grown on yeast extract-peptone-dextrose (YPD) + G418 plates at 30°C. Multiple single colonies were cultured and streaked on YPD to ensure the loss of pCAS-sgRNA<sup>FLAG</sup> plasmid. The *SRP101-FLAG* strain was verified using PCR and DNA sequencing.

To generate the *srp101<sup>dM</sup>-FLAG* strain, pCAS-sgRNA<sup>dM</sup> plasmid encoding a guide RNA sequence (5'-GTTGGTAGTGGGAGAAAG TG-3') was designed to target nucleotide 626 in the *SRP101* coding sequence (5 bp into the MoRF region). To prepare the repair DNA fragment, the coding sequence for the MoRF (residues 208–230) in pUC19-*SRP101-FLAG* was replaced by that for a (GS)<sub>6</sub> linker, and synonymous codon substitutions were introduced at the sequence targeted by the sgRNA<sup>dM</sup> guide sequence using QuikChange Mutagenesis. The *srp101<sup>dM</sup>-FLAG* coding sequence and the flanking 5' UTR and 3' UTR were amplified to produce the linear repair DNA fragment. pCAS-sgRNA<sup>dM</sup> plasmid and the linear repair fragment were cotransformed into the *SRP101-FLAG* strain and grown on YPD + G418 plates. To prevent adaptation of yeast cells to the MoRF deletion (Ogg et al., 1992; Mutka and Walter, 2001), transformed colonies were picked as soon as they reached ~0.5 mm in diameter. All the subsequent culturing of *srp101<sup>dM</sup>* cells were performed in synthetic minimal media with ethanol and glycerol (SCEG). The same procedure was used to generate a WT

control *SRP101-FLAG* strain that contains the same synonymous mutation at the sgRNA<sup>dM</sup> region as the *srp101<sup>dM</sup>-FLAG* strain. Both *SRP101-FLAG* and *srp101<sup>dM</sup>-FLAG* strains were verified by DNA sequencing and were stored and grown in SCEG unless otherwise specified.

### Yeast growth assay

2-ml cultures of *SRP101-FLAG* and *srp101<sup>dM</sup>-FLAG* cells were grown at 30°C in SCEG to OD<sub>600</sub> ~0.6. The cells were then diluted to OD<sub>600</sub> ~0.1, and 2 μl aliquots of 10-fold serial dilutions were spotted onto YPD plates and incubated at 30°C or 37°C for 2 d.

### In vivo pulse-chase assay

*SRP101-FLAG* and *srp101<sup>dM</sup>-FLAG* cells were transformed with a pRS316 vector expressing either 3×HA-DHcA or 3×HA-BirA-Bosl-opsin under the GPD promoter. Transformed cells were grown in SCEG without uracil (-Ura) to OD<sub>600</sub> ~0.4. The cells were then washed and shifted to synthetic defined media (SD) without uracil (-Ura) and grown at 30°C for 3.5 h (Jiang et al., 2008). Yeast cells were harvested, washed in SD(-Ura-Cys-Met), resuspended in 1 ml SD(-Ura-Cys-Met) to a final density of OD<sub>600</sub> ~12, and incubated at 30°C for 30 min. Cells were pulse labeled with 100 μCi/ml EasyTag EXPRESS35S protein labeling mix (PerkinElmer) for 2 min and chased with 1 ml SD(-Ura) supplemented with 10 mM cold methionine and 0.5 mM cysteine. 400-μl aliquots were flash frozen in liquid nitrogen at indicated chase time points.

HA-tagged substrate proteins were immunoprecipitated as described previously (Cho and Shan, 2018). In brief, individual aliquots of cells were harvested and treated with 0.3 M NaOH for 3 min at room temperature, washed with water, and lysed in lysis buffer (20 mM Tris-HCl, pH 8.0, 150 mM NaCl, and 2% SDS) by incubating at 65°C for 15 min. Clarified lysate was diluted 20-fold in anti-HA immunoprecipitation buffer (20 mM Tris-HCl, pH 8.0, 150 mM NaCl, and 1% Triton X-100) before loading on to pre-equilibrated anti-HA magnetic beads (Thermo Fisher Scientific). Following incubation at room temperature for 10 min, the beads were washed with W1 (20 mM Tris-HCl, pH 8.0, 150 mM NaCl, 1% Triton X-100, and 2 M urea), W2 (20 mM Tris-HCl, pH 8.0, 500 mM NaCl, and 1% Triton X-100), W3 (20 mM Tris-HCl, pH 8.0, 150 mM NaCl, and 0.1% SDS), and W4 (20 mM Tris-HCl, pH 8.0, and 150 mM NaCl). Proteins were eluted by adding 10 μl of 1× SDS buffer and boiling for 5 min and analyzed by SDS-PAGE and autoradiography. Translocation efficiency was quantified using Eq. 2, in which  $I_{\text{Protein}}$  and  $I_{\text{gProtein}}$  are the integrated intensities for the protein substrate and glycosylated protein bands, respectively:

$$\% \text{ translocation} = \frac{I_{\text{gProtein}}}{I_{\text{gProtein}} + I_{\text{Protein}}} \times 100. \quad (2)$$

### Western blot

Yeast microsomes were isolated from *SRP101-FLAG* and *srp101<sup>dM</sup>-FLAG* strains as described (Rao et al., 2016). In brief, yeast spheroplasts were made by incubating harvested cells with

0.4 mg lyticase per units of OD<sub>600</sub> of cells at 30°C for ~35 min in spheroplast buffer (50 mM Hepes, pH 7.4, 2% glucose, 0.22 g/ml sorbitol, 0.01 g/ml yeast extract, and 0.1 g/ml peptone). The spheroplast reaction was quenched on ice and cleaned up through a 1.5% Ficoll 400 cushion. The spheroplasts were re-suspended in sorbitol lysis buffer (0.02 g/ml sorbitol, 50 mM Hepes, pH 7.4, 50 mM KOAc, 2 mM EDTA, 1 mM DTT, and 1× protease inhibitor cocktail) using a homogenizer. ER microsomes were then purified from lysed spheroplasts through a 1-M sucrose cushion. Purified and washed ER microsomes were pelleted, resuspended to a final concentration of 50–100 U/ml, aliquoted, and flash frozen until ready. Microsome aliquots were boiled for 5 min in 2× SDS buffer immediately after thawing. 0.5–1 units of microsomes were analyzed by SDS-PAGE and immunoblotting using anti-FLAG antibody (Genscript). IRDye 800CW goat anti-mouse secondary antibody (LI-COR Biosciences) was used for visualization on an Odyssey imaging system.

### GTPase assay

GTPase reactions were performed in SRP assay buffer (50 mM KHepes, pH 7.5, 200 mM KOAc, 5 mM Mg(OAc)<sub>2</sub>, 10% glycerol, 2 mM DTT, and 0.02% Nikkol) at 25°C. Reactions were followed and analyzed as described previously (Lee et al., 2018). The reciprocally stimulated GTPase reactions between SRP and SR were measured under multiple turnover conditions using 0.15 μM SRP(4A10L) and 0.2 μM 80S when indicated, varying concentrations of SR, and 100 μM GTP doped with trace γ-<sup>32</sup>P-GTP (PerkinElmer). The SR concentration dependences of observed rate constants ( $k_{obsd}$ ) were fitted to Eq. 3, where  $k_{cat}$  is the GTPase rate constant at saturating SR concentration and  $K_m$  is the SR concentration required to reach half of the maximal observed GTPase rate constant:

$$k_{obsd} = k_{cat} \times \frac{[SR]}{K_m + [SR]} \quad (3)$$

### Fluorescence FRET measurements

All reactions were measured in SRP buffer supplemented with 0.03% BSA and 0.04% Nikkol at 25°C. All fluorescence measurements used SRs carrying the R458A mutation, which specifically blocks GTP hydrolysis, to enable measurements of the assembly and disassembly of SRP and SR in their GTP-bound state. The values of  $k_{off}$  were determined using pulse-chase experiments on a stopped-flow apparatus (Kintek) with WT SR and a Fluorolog 3-22 spectrofluorometer (Jobin Yvon) with mutant SRs. The SRP·SR complexes were preformed using 12.5 nM labeled SRP(4A10L) and 1 μM WT or mutant SR in the presence of 1 mM GTP, plus 50 nM 80S when indicated. 8 μM unlabeled WT SR was added to initiate complex dissociation. Nonspecific fluorescence change was corrected by subtracting the background signal change measured in a parallel reaction in which the same volume of buffer was added. The time courses of fluorescence change were fitted to Eq. 4 (for WT SR in the presence of ribosome) or Eq. 5 (for all other conditions) to extract the dissociation rate constants ( $k_{off}$ ).  $F_{obsd}$  is the measured donor

fluorescence signal,  $F_{AMP}$  is the corrected fluorescence change,  $F_0$  is the initial fluorescence value at time zero, and  $t$  is time:

$$F_{obsd} = F_{AMP} [1 - \exp(-k_{off1}t) - \exp(-k_{off2}t)] + F_0, \quad (4)$$

$$F_{obsd} = F_{AMP} [1 - \exp(-k_{off}t)] + F_0. \quad (5)$$

The equilibrium  $K_d$  of SRP·SR complexes were measured on a Fluorolog 3-22 spectrofluorometer. The equilibrium titrations were performed using 12.5 nM Cy3B-labeled SRP, 1 mM GTP, and addition of increasing concentrations of Atto647N-labeled WT or mutant SR. Donor fluorescence was recorded when equilibrium was reached. The signal change was corrected by subtracting the background signal of a control titration with unlabeled SR WT/mutants performed in parallel. The fluorescence signal was converted to FRET efficiency ( $E$ ) according to Eq. 6,

$$E = 1 - \frac{F_{DA}}{F_{DO}}, \quad (6)$$

in which  $F_{DO}$  and  $F_{DA}$  are fluorescence signals in the absence and presence of the acceptor, respectively. The SR concentration dependences of  $E$  were fitted to Eq. 7 to extract the values of  $K_d$ .  $E_{max}$  is the value of  $E$  at saturating SR concentration:

$$E = E_{max} \times \frac{[SR]}{K_d + [SR]}. \quad (7)$$

### SR-80S cosedimentation assay

Binding reactions were performed in 50 mM KHepes, pH 7.5, 100 mM KOAc, 5 mM Mg(OAc)<sub>2</sub>, and 1 mM DTT at 25°C. 400 nM SR was incubated with 150 nM 80S in a 50-μl reaction for 10 min. The mixture was loaded onto a 110 μl 1 M sucrose cushion and ultracentrifuged at 100,000 rpm for 2 h in a TLA100 rotor (Beckman Coulter). The pellet fractions were re-suspended in 20 μl of 1× SDS loading buffer. Equal amounts of the total and pellet samples were analyzed on 10% SDS-PAGE gels. The gels were Coomassie stained and scanned on a LI-COR Odyssey imager using a wavelength of 700 nm, and the intensities of the bands of interest were quantified. For SR-Xβ and SR-NG, which do not resolve well from ribosomal proteins, the N-terminally His<sub>6</sub>-tagged SRα bands were detected by Western blot using anti-His<sub>5</sub> mouse antibody (Abcam) and IRDye 800CW goat anti-mouse IgG (H + L; LI-COR), and quantified on the LI-COR Odyssey imager.

### Online supplemental material

Fig. S1 shows the sequence alignment of eukaryotic SRα. Fig. S2 shows additional *in vivo* characterizations of yeast cells harboring the SRdM mutation. Fig. S3 shows characterizations of SR linker mutants in the SRdX construct. Fig. S4 shows replicates of the cosedimentation experiments to measure the binding of SR to the ribosome. Fig. S5 shows the SR concentration dependences of the stimulated GTPase reactions for SRPs harboring mutations in 7SL RNA and for mutant SR-K537.

## Acknowledgments

We thank the Shan laboratory members for valuable suggestions and H. Bernstein for sharing canine pancreatic microsomes.

This work was supported by National Institutes of Health grant GM078024 and Gordon and Betty Moore Foundation GBMF2939 to S.-o. Shan.

The authors declare no competing financial interests.

Author contributions: Y.-H. Hwang Fu and S.-o. Shan designed research; Y.-H. Hwang Fu, S. Chandrasekar, and S.-o. Shan performed research; Y.-H. Hwang Fu, S. Chandrasekar, and J.H. Lee contributed new reagents/analytic tools; Y.-H. Hwang Fu, S. Chandrasekar, and S.-o. Shan analyzed data; Y.-H. Hwang Fu and S.-o. Shan wrote the paper; S.-o. Shan supervised the project.

Submitted: 1 January 2019

Revised: 28 June 2019

Accepted: 26 August 2019

## References

- Akopian, D., K. Shen, X. Zhang, and S.O. Shan. 2013. Signal recognition particle: an essential protein-targeting machine. *Annu. Rev. Biochem.* 82: 693–721. <https://doi.org/10.1146/annurev-biochem-072711-164732>
- Ataide, S.F., N. Schmitz, K. Shen, A. Ke, S.O. Shan, J.A. Doudna, and N. Ban. 2011. The crystal structure of the signal recognition particle in complex with its receptor. *Science*. 331:881–886. <https://doi.org/10.1126/science.1196473>
- Bacher, G., H. Lütcke, B. Jungnickel, T.A. Rapoport, and B. Dobberstein. 1996. Regulation by the ribosome of the GTPase of the signal-recognition particle during protein targeting. *Nature*. 381:248–251. <https://doi.org/10.1038/381248a0>
- Bacher, G., M. Pool, and B. Dobberstein. 1999. The ribosome regulates the GTPase of the  $\beta$ -subunit of the signal recognition particle receptor. *J. Cell Biol.* 146:723–730. <https://doi.org/10.1083/jcb.146.4.723>
- Beckert, B., A. Kedrov, D. Sohmen, G. Kempf, K. Wild, I. Sinning, H. Stahlberg, D.N. Wilson, and R. Beckmann. 2015. Translational arrest by a prokaryotic signal recognition particle is mediated by RNA interactions. *Nat. Struct. Mol. Biol.* 22:767–773. <https://doi.org/10.1038/nsmb.3086>
- Beitz, E. 2000. TEXshade: shading and labeling of multiple sequence alignments using LATEX2 epsilon. *Bioinformatics*. 16:135–139. <https://doi.org/10.1093/bioinformatics/16.2.135>
- Cho, H., and S.O. Shan. 2018. Substrate relay in an Hsp70-cochaperone cascade safeguards tail-anchored membrane protein targeting. *EMBO J.* 37: e99264. <https://doi.org/10.15252/embj.201899264>
- Cumberworth, A., G. Lamour, M.M. Babu, and J. Gsponer. 2013. Promiscuity as a functional trait: intrinsically disordered regions as central players of interactomes. *Biochem. J.* 454:361–369. <https://doi.org/10.1042/BJ20130545>
- Disfani, F.M., W.L. Hsu, M.J. Mizianty, C.J. Oldfield, B. Xue, A.K. Dunker, V.N. Uversky, and L. Kurgan. 2012. MoRFPred, a computational tool for sequence-based prediction and characterization of short disorder-to-order transitioning binding regions in proteins. *Bioinformatics*. 28: i75–i83. <https://doi.org/10.1093/bioinformatics/bts209>
- Fang, C., T. Noguchi, D. Tominaga, and H. Yamana. 2013. MFSPSSMPred: identifying short disorder-to-order binding regions in disordered proteins based on contextual local evolutionary conservation. *BMC Bioinformatics*. 14:300. <https://doi.org/10.1186/1471-2105-14-300>
- Fersht, A. 1999. *Structure and Mechanism in Protein Science: A Guide to Enzyme Catalysis and Protein Folding*. W.H. Freeman, New York. 650 pp.
- Fulga, T.A., I. Sinning, B. Dobberstein, and M.R. Pool. 2001. SRbeta coordinates signal sequence release from SRP with ribosome binding to the translocon. *EMBO J.* 20:2338–2347. <https://doi.org/10.1093/emboj/20.9.2338>
- Fung, H.Y.J., M. Birol, and E. Rhoades. 2018. IDPs in macromolecular complexes: the roles of multivalent interactions in diverse assemblies. *Curr. Opin. Struct. Biol.* 49:36–43. <https://doi.org/10.1016/j.sbi.2017.12.007>
- Halic, M., M. Gartmann, O. Schlenker, T. Mielke, M.R. Pool, I. Sinning, and R. Beckmann. 2006. Signal recognition particle receptor exposes the ribosomal translocon binding site. *Science*. 312:745–747. <https://doi.org/10.1126/science.1124864>
- Hortsch, M., D. Avossa, and D.I. Meyer. 1985. A structural and functional analysis of the docking protein. Characterization of active domains by proteolysis and specific antibodies. *J. Biol. Chem.* 260:9137–9145.
- Jadhav, B., M. McKenna, N. Johnson, S. High, I. Sinning, and M.R. Pool. 2015. Mammalian SRP receptor switches the Sec61 translocase from Sec62 to SRP-dependent translocation. *Nat. Commun.* 6:10133. <https://doi.org/10.1038/ncomms10133>
- Jiang, Y., Z. Cheng, E.C. Mandon, and R. Gilmore. 2008. An interaction between the SRP receptor and the translocon is critical during cotranslational protein translocation. *J. Cell Biol.* 180:1149–1161. <https://doi.org/10.1083/jcb.200707196>
- Kobayashi, K., A. Jomaa, J.H. Lee, S. Chandrasekar, D. Boehringer, S.O. Shan, and N. Ban. 2018. Structure of a prehandover mammalian ribosomal SRP-SRP receptor targeting complex. *Science*. 360:323–327. <https://doi.org/10.1126/science.aar7924>
- Latysheva, N.S., T. Flock, R.J. Weatheritt, S. Chavali, and M.M. Babu. 2015. How do disordered regions achieve comparable functions to structured domains? *Protein Sci.* 24:909–922. <https://doi.org/10.1002/pro.2674>
- Lauffer, L., P.D. Garcia, R.N. Harkins, L. Coussens, A. Ullrich, and P. Walter. 1985. Topology of signal recognition particle receptor in endoplasmic reticulum membrane. *Nature*. 318:334–338. <https://doi.org/10.1038/318334a0>
- Lee, J.H., S. Chandrasekar, S. Chung, Y.H. Hwang Fu, D. Liu, S. Weiss, and S.O. Shan. 2018. Sequential activation of human signal recognition particle by the ribosome and signal sequence drives efficient protein targeting. *Proc. Natl. Acad. Sci. USA*. 115:E5487–E5496. <https://doi.org/10.1073/pnas.1802252115>
- Legate, K.R., and D.W. Andrews. 2003. The  $\beta$ -subunit of the signal recognition particle receptor is a novel GTP-binding protein without intrinsic GTPase activity. *J. Biol. Chem.* 278:27712–27720. <https://doi.org/10.1074/jbc.M302158200>
- Mandon, E.C., Y. Jiang, and R. Gilmore. 2003. Dual recognition of the ribosome and the signal recognition particle by the SRP receptor during protein targeting to the endoplasmic reticulum. *J. Cell Biol.* 162:575–585. <https://doi.org/10.1083/jcb.200303143>
- Mary, C., A. Scherrer, L. Huck, A.K. Lakkaraju, Y. Thomas, A.E. Johnson, and K. Strub. 2010. Residues in SRP9/14 essential for elongation arrest activity of the signal recognition particle define a positively charged functional domain on one side of the protein. *RNA*. 16:969–979. <https://doi.org/10.1261/rna.2040410>
- Mészáros, B., I. Simon, and Z. Dosztányi. 2009. Prediction of protein binding regions in disordered proteins. *PLOS Comput. Biol.* 5:e1000376. <https://doi.org/10.1371/journal.pcbi.1000376>
- Meyer, D.I., and B. Dobberstein. 1980. A membrane component essential for vectorial translocation of nascent proteins across the endoplasmic reticulum: requirements for its extraction and reassociation with the membrane. *J. Cell Biol.* 87:498–502. <https://doi.org/10.1083/jcb.87.2.498>
- Mohan, A., C.J. Oldfield, P. Radivojac, V. Vacic, M.S. Cortese, A.K. Dunker, and V.N. Uversky. 2006. Analysis of molecular recognition features (MoRFs). *J. Mol. Biol.* 362:1043–1059. <https://doi.org/10.1016/j.jmb.2006.07.087>
- Mutka, S.C., and P. Walter. 2001. Multifaceted physiological response allows yeast to adapt to the loss of the signal recognition particle-dependent protein-targeting pathway. *Mol. Biol. Cell.* 12:577–588. <https://doi.org/10.1091/mbc.12.3.577>
- Ng, D.T.W., J.D. Brown, and P. Walter. 1996. Signal sequences specify the targeting route to the endoplasmic reticulum membrane. *J. Cell Biol.* 134: 269–278. <https://doi.org/10.1083/jcb.134.2.269>
- Notredame, C., D.G. Higgins, and J. Heringa. 2000. T-Coffee: A novel method for fast and accurate multiple sequence alignment. *J. Mol. Biol.* 302: 205–217. <https://doi.org/10.1006/jmbi.2000.4042>
- Ogg, S.C., M.A. Poritz, and P. Walter. 1992. Signal recognition particle receptor is important for cell growth and protein secretion in *Saccharomyces cerevisiae*. *Mol. Biol. Cell.* 3:895–911. <https://doi.org/10.1091/mbc.3.8.895>
- Ogg, S.C., W.P. Barz, and P. Walter. 1998. A functional GTPase domain, but not its transmembrane domain, is required for function of the SRP receptor beta-subunit. *J. Cell Biol.* 142:341–354. <https://doi.org/10.1083/jcb.142.2.341>

- Oldfield, C.J., and A.K. Dunker. 2014. Intrinsically disordered proteins and intrinsically disordered protein regions. *Annu. Rev. Biochem.* 83: 553–584. <https://doi.org/10.1146/annurev-biochem-072711-164947>
- Oldfield, C.J., Y. Cheng, M.S. Cortese, C.J. Brown, V.N. Uversky, and A.K. Dunker. 2005. Comparing and combining predictors of mostly disordered proteins. *Biochemistry.* 44:1989–2000. <https://doi.org/10.1021/bi047993o>
- Oldfield, C.J., J. Meng, J.Y. Yang, M.Q. Yang, V.N. Uversky, and A.K. Dunker. 2008. Flexible nets: disorder and induced fit in the associations of p53 and 14-3-3 with their partners. *BMC Genomics.* 9(Suppl 1):S1. <https://doi.org/10.1186/1471-2164-9-S1-S1>
- Peluso, P., D. Herschlag, S. Nock, D.M. Freymann, A.E. Johnson, and P. Walter. 2000. Role of 4.5S RNA in assembly of the bacterial signal recognition particle with its receptor. *Science.* 288:1640–1643. <https://doi.org/10.1126/science.288.5471.1640>
- Peluso, P., S.O. Shan, S. Nock, D. Herschlag, and P. Walter. 2001. Role of SRP RNA in the GTPase cycles of Ffh and FtsY. *Biochemistry.* 40:15224–15233. <https://doi.org/10.1021/bi011639y>
- Rao, M., V. Okreglak, U.S. Chio, H. Cho, P. Walter, and S.O. Shan. 2016. Multiple selection filters ensure accurate tail-anchored membrane protein targeting. *eLife.* 5:e21301. <https://doi.org/10.7554/eLife.21301>
- Ryan, O.W., S. Poddar, and J.H.D. Cate. 2016. Crispr-cas9 genome engineering in *Saccharomyces cerevisiae* cells. *Cold Spring Harb. Protoc.* 2016: 525–533. <https://doi.org/10.1101/pdb.prot086827>
- Shan, S.O. 2016. ATPase and GTPase Tangos Drive Intracellular Protein Transport. *Trends Biochem. Sci.* 41:1050–1060. <https://doi.org/10.1016/j.tibs.2016.08.012>
- Shen, K., and S.O. Shan. 2010. Transient tether between the SRP RNA and SRP receptor ensures efficient cargo delivery during cotranslational protein targeting. *Proc. Natl. Acad. Sci. USA.* 107:7698–7703. <https://doi.org/10.1073/pnas.1002968107>
- Shen, K., X. Zhang, and S.O. Shan. 2011. Synergistic actions between the SRP RNA and translating ribosome allow efficient delivery of the correct cargos during cotranslational protein targeting. *RNA.* 17:892–902. <https://doi.org/10.1261/rna.2610411>
- van der Lee, R., M. Buljan, B. Lang, R.J. Weatheritt, G.W. Daughdrill, A.K. Dunker, M. Fuxreiter, J. Gough, J. Gsponer, D.T. Jones, et al. 2014. Classification of intrinsically disordered regions and proteins. *Chem. Rev.* 114:6589–6631. <https://doi.org/10.1021/cr400525m>
- Wang, F., E.C. Brown, G. Mak, J. Zhuang, and V. Denic. 2010. A chaperone cascade sorts proteins for posttranslational membrane insertion into the endoplasmic reticulum. *Mol. Cell.* 40:159–171. <https://doi.org/10.1016/j.molcel.2010.08.038>
- Ward, J.J., J.S. Sodhi, L.J. McGuffin, B.F. Buxton, and D.T. Jones. 2004. Prediction and functional analysis of native disorder in proteins from the three kingdoms of life. *J. Mol. Biol.* 337:635–645. <https://doi.org/10.1016/j.jmb.2004.02.002>
- Wright, P.E., and H.J. Dyson. 2015. Intrinsically disordered proteins in cellular signalling and regulation. *Nat. Rev. Mol. Cell Biol.* 16:18–29. <https://doi.org/10.1038/nrm3920>
- Yabal, M., S. Brambillasca, P. Soffientini, E. Pedrazzini, N. Borgese, and M. Makarow. 2003. Translocation of the C terminus of a tail-anchored protein across the endoplasmic reticulum membrane in yeast mutants defective in signal peptide-driven translocation. *J. Biol. Chem.* 278: 3489–3496. <https://doi.org/10.1074/jbc.M210253200>
- Zhang, X., and S.O. Shan. 2014. Fidelity of cotranslational protein targeting by the signal recognition particle. *Annu. Rev. Biophys.* 43:381–408. <https://doi.org/10.1146/annurev-biophys-051013-022653>
- Zhang, X., S. Kung, and S.O. Shan. 2008. Demonstration of a multistep mechanism for assembly of the SRP x SRP receptor complex: implications for the catalytic role of SRP RNA. *J. Mol. Biol.* 381:581–593. <https://doi.org/10.1016/j.jmb.2008.05.049>